Ab initio modeling of quasielastic neutron scattering of hydrogen pipe diffusion in palladium

Emily J. Schiavone and Dallas R. Trinkle*

Department of Materials Science and Engineering, University of Illinois, Urbana-Champaign, Illinois 61801, USA

(Received 18 May 2016; published 26 August 2016)

A recent quasielastic neutron scattering (QENS) study of hydrogen in heavily deformed fcc palladium provided the first direct measurement of hydrogen pipe diffusion, which has a significantly higher diffusivity and lower activation barrier than in bulk. While *ab initio* estimates of hydrogen diffusion near a dislocation corroborated the experimental values, open questions remain from the Chudley-Elliott analysis of the QENS spectra, including significant nonmonotonic changes in jump distance with temperature. We calculate the spherically averaged incoherent scattering function at different temperatures using our *ab initio* data for the network of site energies, jump rates, and jump vectors to directly compare to experiment. Diffusivities and jump distances are sensitive to how a single Lorentzian is fit to the scattering function. Using a logarithmic least squares fit over the range of experimentally measured energies, our diffusivities and jump distances agree well with those measured by experiment. However, these calculated quantities do not reflect barriers or distances in our dislocation geometry. This computational approach allows for validation against experiment, along with a more detailed understanding of the QENS results.

DOI: 10.1103/PhysRevB.94.054114

I. INTRODUCTION

Dislocation pipe diffusion, which is accelerated diffusion along a dislocation relative to diffusion in bulk, has been proposed to explain accelerated diffusion in some deformed materials [1–3]. Volin *et al.* found direct evidence of dislocation pipe diffusion using transmission electron microscopy (TEM), which measured the size of voids connected to dislocations in aluminum at different annealing stages and found accelerated diffusion along the dislocation compared to diffusion into the bulk [4]. Tang *et al.* used TEM to study dislocation dipole annihilation in undoped and MgO-doped sapphire and estimated pipe diffusion coefficients assuming that the oxygen and aluminum point defects traveled along the dislocation to create dislocation loops [5]. Legros *et al.* used TEM to measure an accelerated dissolution rate of silicon precipitates connected by a dislocation in an aluminum thin film and extracted a pipe diffusion energy barrier [6]. However, dislocations do not always lead to faster diffusion; one computational study used an embedded-atom model potential and found reduced hydrogen diffusion along both screw and edge dislocations in Fe due to high diffusion barriers [7]. Previous studies of hydrogen near a palladium dislocation found the formation of hydrides in the dislocation core [8], which could block pipe diffusion. Heuser *et al.* directly measured with quasielastic neutron scattering (QENS) increased diffusivity and an energy barrier for hydrogen pipe diffusion in deformed palladium [9]. Spectra of the incoherent scattering function $S_{\text{inc}}(Q,\omega)$ as a function of frequency ω from QENS experiments are fit with a single Lorentzian, or sometimes a sum of two or more Lorentzians, for a given magnitude of the wave vector Q. The Lorentzian widths as a function of Q can be fit with a Chudley-Elliott (CE) model [10] to extract jump distances and mean residence times, which yield diffusivities. Using this fitting approach, Heuser *et al.* found diffusion barriers lower than those predicted by density functional theory (DFT) calculations. In addition, the jump distances were much larger than bulk jump distances and nonmonotonic as a function of temperature.

A number of studies have attempted to calculate the incoherent scattering function and have show this to be difficult. Li and Wahnström used molecular dynamics with an embedded-atom method potential to calculate the intermediate scattering function from the self-correlation function for hydrogen in bulk palladium [11,12]. Comparison with experimental results required a temporal Fourier transform of the intermediate scattering function to produce the incoherent scattering function. To transform the intermediate function, the authors introduced a dampening factor with an adjustable parameter to smooth out the intermediate scattering function. To better match experimental results [13], these authors introduced an adjustable parameter friction coefficient based on first principles calculations of hydrogen in a homogeneous electron gas [12]. Gillan used a similar approach for hydrogen in palladium using a pair potential and also failed to find agreement with experiment [14]. Björketun *et al.* used DFT-informed kinetic Monte Carlo (KMC) simulations to calculate incoherent scattering of a proton in a disordered perovskite structure, but failed to recover a Q^2 law for small Q [15]. Rowe *et al.* developed an analytic solution for diffusion through a network of energetically equivalent octahedral and tetrahedral sites in a body centered cubic lattice [16]. Building upon this method, Kehr *et al.* computed the incoherent scattering function for one-dimensional lattices with inequivalent site energies [17]. A generalized version of this method has been developed to calculate the incoherent scattering function from an arbitrary diffusion network [18–21], but this approach has not been applied to study hydrogen diffusion near a dislocation.

We use DFT to compute site energies and energy barriers of hydrogen in a palladium edge dislocation geometry from which we calculate the incoherent scattering function using the generalized analytic method mentioned above. We consider only an edge dislocation, as it has the strongest binding with hydrogen, and hence at low concentrations and temperatures produce the dominant signal. The analysis allows for direct

*dtrinkle@illinois.edu

comparison with QENS data [9]. We also follow the same fitting procedures as a typical QENS experiment [22] by fitting the incoherent scattering function versus energy to a single Lorentzian, extracting the half width at half maximum, and fitting these widths as a function of Q to a CE model. We try several fitting schemes that each produce different values for diffusivities and jump distances. We find that the typical fitting procedure introduces unphysical jump distances and underestimates the diffusion barrier along the dislocation.

II. EVALUATING THE INCOHERENT SCATTERING FUNCTION

A. Site energies, jump vectors, and jump rates

We perform DFT calculations using the plane-wave basis code VASP [23,24]. We use projector augmented wave (PAW) potentials [25] generated by Kresse [26] with s valence for H, s and d valence electronic configurations for Pd, and the local density approximation for the exchange-correlation energy. For the dislocation geometry, we use a plane-wave energy cutoff of 250 eV, a $1 \times 1 \times 8$ k-point grid, a Methfessel-Paxton smearing width of 0.25 eV, and a force convergence of 5 meV/Å. These settings are identical to those chosen by Lawler and Trinkle [27] and Trinkle *et al.* [8] for simulating H near a Pd edge dislocation. For hydrogen in bulk palladium, we use a $6 \times 6 \times 6$ k-point grid and an energy cutoff of 300 eV for our supercell containing 256 Pd atoms and one H interstitial. We calculate the equilibrium lattice parameter to be 3.852 Å, which is slightly smaller than the experimental value of 3.872 Å at 4.2 K [28]. Previous DFT studies [29] found that hydrogen in bulk palladium diffuses from a ground state octahedral site to a tetrahedral site into another octahedral site. We perform climbing image nudged elastic band [30] calculations with a single image to compute the configurations and energies of the transition states. Our DFT calculated activation energy $E_{\mathrm{OT}} = 0.277$ eV for a hydrogen interstitial to transition from an octahedral site to a tetrahedral site in bulk palladium agrees well with the experimental value 0.230 eV [31].

An edge dislocation volumetrically strains interstitial sites near the dislocation core, which leads to lower diffusion barriers between expanded sites in palladium. We use a 382-atom palladium edge dislocation geometry with a $[\bar{1}\bar{1}0]$ Burgers vector that is periodic along the $[1\bar{1}2]$ threading direction. The palladium edge dislocation geometry is the same as in Refs. [8,27]. We define the site energies of the interstitial sites in the dislocation relative to bulk as

$$E_{\mathrm{interstitial}} = E_{\mathrm{disl+H}} - E_{\mathrm{disl}} - (E_{\mathrm{bulk+H}} - E_{\mathrm{bulk}}), \qquad (1)$$

where $E_{\mathrm{disl+H}}$ is the energy of hydrogen in an interstitial site in the dislocation geometry, E_{disl} is the energy of the dislocation without hydrogen, $E_{\mathrm{bulk+H}}$ is the energy of hydrogen in a bulk interstitial site, and E_{bulk} is the energy of bulk palladium without hydrogen. The ground state of hydrogen in the dislocation geometry is an octahedral site directly below the partial core, which has a site energy of -0.125 eV relative to an octahedral site in bulk [9]. We expect lowered barriers and thus accelerated diffusion in expanded sites below the partial core. While we do find a pathway with lower barriers below the partial core, the barrier to diffuse along this path, 0.151 eV, is higher than observed in experiment [9], 0.083 ± 0.005 eV for a hydrogen concentration of 1.13×10^{-3} and 0.042 ± 0.012 eV for a hydrogen concentration of 0.52×10^{-3}. We find a pathway inside the partial core (cf. Fig. 1) with a lower barrier of 0.111 eV. However, this barrier is still higher than those measured by experiment.

Figure 1 compares hydrogen diffusion paths along the $[1\bar{1}2]$ threading direction directly below [Fig. 1(c)] and inside the dislocation partial core [Fig. 1(d)] to a diffusion path along the same direction in bulk palladium [Figs. 1(a) and 1(b)]. The path below the partial core is expanded but still looks bulklike. The highly distorted pathway inside the partial cores looks significantly different than the bulk pathway. The two $\frac{a}{6}\langle 211\rangle$ partial cores separate the face centered cubic structure outside the core region from the hexagonal close packed structure in the stacking fault. This transition between structures creates sheared sites in the partial cores that are neither octahedral nor tetrahedral. While some sites in the core become unstable

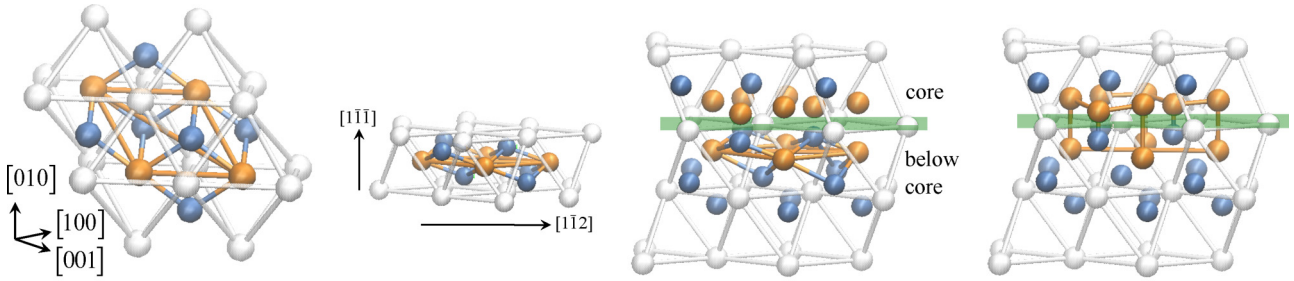

FIG. 1. Geometries of hydrogen diffusion pathways. (a) The network for hydrogen diffusion between two octahedral interstitial sites (orange) along the $[1\bar{1}2]$ direction in fcc Pd includes two additional nearest neighbor octahedral interstitial sites along [110]-type directions and six tetrahedral interstitial sites (blue). (b) The bulk network reoriented with the threading direction and slip plane normal of the edge dislocation shown. (c) The (partial) dislocation maintains periodicity along the $[1\bar{1}2]$ threading direction. The network connecting two nearest neighbor octahedral sites along the $[1\bar{1}2]$ direction of the dislocation supercell in the expanded region directly below the partial core looks similar to the bulk network. The green slip plane is $(1\bar{1}\bar{1})$. (d) The lowest energy pathway through the periodic direction of the dislocation lies in the core of the partial dislocation. Here the distinction between octahedral and tetrahedral sites becomes blurred. The orange sites have low site energies—similar to octahedral sites—and the blue sites have high site energies—similar to tetrahedral sites.

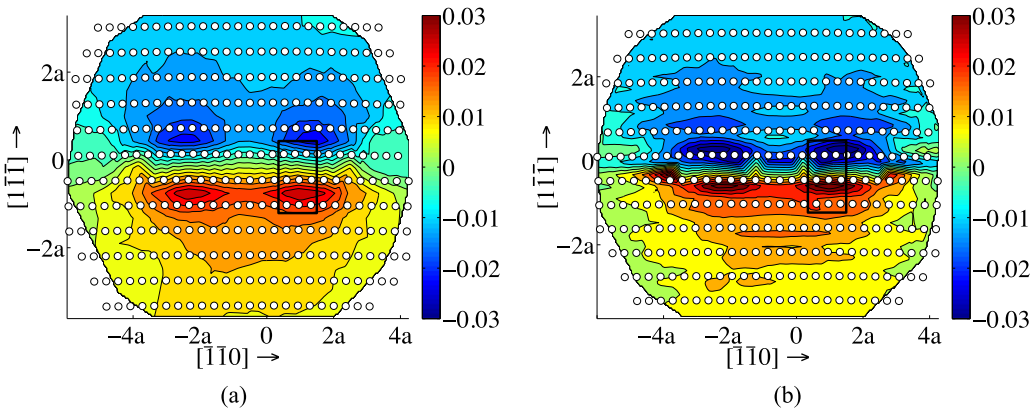

FIG. 2. Volumetric strain of (a) octahedral interstitial and (b) tetrahedral interstitial sites in an $\frac{a}{2}[110]$ edge dislocation that has split into partials. The extra half plane is located on the top half of the figure, and the Burgers vector points along [110]. The black boxes outline the palladium atoms and interstitial sites included in Figs. 1(c) and 1(d). The dislocation geometry is periodic along the [1$\bar{1}$2] threading direction, pointing out of the page [in contrast to Figs. 1(c) and 1(d), in which the threading direction points to the right]. This dislocation has split into two partials in the (1$\bar{1}\bar{1}$) slip plane. The sites with the largest tensile strain are located beneath the partial cores.

or have high site energies, most of the sites have energies ∼0.03–0.06 eV above the ground state. Diffusion pathways through these sites along the threading direction do not pass through higher energy tetrahedral sites as they do in the bulk. The barriers to diffuse from the expanded region below the core into the core are low, as small as 0.048 eV, while the barrier out of the core is 0.041 eV.

Figure 2 compares the distributions of volumetric strain due to the dislocation for octahedral and tetrahedral interstitial sites that lead to inhomogeneous changes in the relative site energies and energy barrier between the differently strained sites. To evaluate the volumetric strain, we first identify the six (four) Pd atoms that define the octahedral (tetrahedral) "cage"; then, we take the center of mass of the cage as the interstitial site, and use the vectors from this site to the neighbors to find the volumetric strain [32]. The extra half plane creates compressive strain above the slip plane and tensile strain below the slip plane for both octahedral and tetrahedral sites. Sites near the partial cores have the largest volumetric strain, with the strain falling off more quickly for the tetrahedral sites than for the octahedral sites. There are only two site energies (E_O and E_T) and two barriers in bulk (E_{OT} and E_{TO}), but the dislocation breaks the symmetry, leading to spatially dependent site energies and barriers. We use DFT to calculate the energetics of hydrogen in highly distorted sites inside the stacking fault, inside the dislocation partial cores, and below the partial cores. However, calculating each site energy and site energy barrier in the dislocation geometry with DFT is computationally expensive, so we develop an approximation for the site energies and energy barriers for sites outside of the partial cores.

Figure 3 shows the linear relationships between energy and small volumetric strains in bulk that we use to model site energies and energy barriers around the dislocation geometry. We calculate site energies of hydrogen in unstrained and ±2% strained bulk using DFT. The linear change in the site energy difference and energy barrier with respect to strain, in the small strain limit (±2%) in bulk, is consistent with previous studies [33]. We compare the site energies calculated with DFT and the approximated site energies for the outermost sites of the expanded region and find good agreement to within 25 meV, which justifies our use of this simple approximation. The transition state—located in a {111} face—is two-thirds along the line from octahedral to tetrahedral site. If we consider octahedral and tetrahedral sites that have different strains, we model the energy barriers as

$$E_{OT}^{\text{hetero}}(\varepsilon_O,\varepsilon_T) = \frac{2}{3}[E_T(\varepsilon_T) - E_O(\varepsilon_O)] + \frac{1}{3}E_{OT}\left(\frac{\varepsilon_T+\varepsilon_O}{2}\right) + \frac{2}{3}E_{TO}\left(\frac{\varepsilon_T+\varepsilon_O}{2}\right) \quad (2)$$

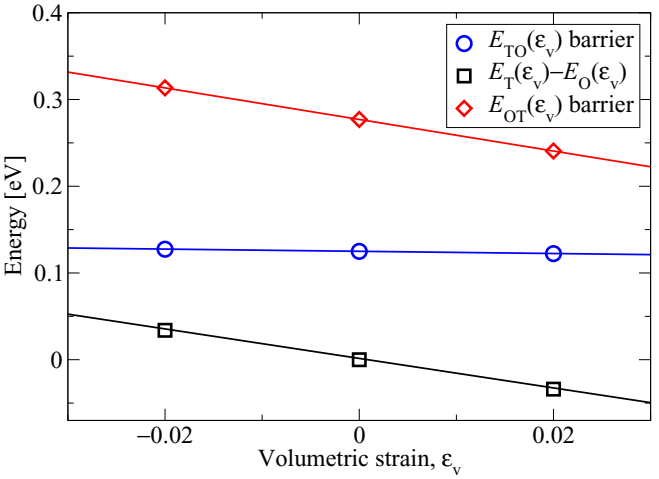

FIG. 3. Strain dependence of bulk octahedral to tetrahedral energy barrier, tetrahedral to octahedral energy barrier, and octahedral and tetrahedral site energy difference. For small strains, site energies and energy barriers computed with DFT vary linearly with respect to strain. The individual site energy differences also vary linearly with respect to strain. We use these simple linear strain dependencies to approximate the site energies and energy barriers for all sites in the dislocation geometry, excluding the highly distorted sites and barriers inside the partial cores and in the stacking fault.

and

$$E_{\mathrm{TO}}^{\mathrm{hetero}}(\varepsilon_{\mathrm{O}},\varepsilon_{\mathrm{T}}) = -\frac{1}{3}[E_{\mathrm{T}}(\varepsilon_{\mathrm{T}}) - E_{\mathrm{O}}(\varepsilon_{\mathrm{O}})] + \frac{1}{3}E_{\mathrm{OT}}\left(\frac{\varepsilon_{\mathrm{T}}+\varepsilon_{\mathrm{O}}}{2}\right) + \frac{2}{3}E_{\mathrm{TO}}\left(\frac{\varepsilon_{\mathrm{T}}+\varepsilon_{\mathrm{O}}}{2}\right), \quad (3)$$

where we use the average of the volumetric strain of the octahedral site ε_{O} and the volumetric strain of the tetrahedral site ε_{T} as the strain of the transition state. To compute the jump rate $\nu_{mn} = \nu_0 \exp(-E_{mn}/k_{\mathrm{B}}T)$ from site m to site n, we use a constant prefactor $\nu_0 = 10^{13}$ s^{-1}.

We use these jump rates along with the site energies and jump vectors as the input for KMC calculations. We run trajectories with 10^4 transitions unless the hydrogen atom jumps outside of the dislocation geometry, at which point we consider it to have escaped. For each temperature, we average 3000 KMC trajectories and calculate diffusivity from the long time limit of the mean squared displacement divided by time. From the computed diffusivities (Fig. 9) over the temperature range 100–500 K, we extract an effective activation barrier for diffusion of $E_a = 0.125$ eV; this is larger than the experimentally modeled activation barrier of 0.042–0.083 eV, extracted from a Chudley-Elliot analysis of incoherent scattering [9]. The deviation from linearity at higher temperatures in the Arrhenius plot indicates changes in the diffusion mechanism as pipe diffusion becomes less dominant at higher temperatures. In addition, KMC simulations do not predict unusual changes in average jump distance with temperature, as the Chudley-Elliot analysis suggests; to explain these discrepancies, we compute the incoherent scattering function.

B. Incoherent scattering function

We construct the incoherent scattering function from site energies, jump rates, and jump vectors of the diffusion network to compare with quasielastic neutron experiments. A generalized expression for incoherent scattering is derived in Ref. [19]; we outline this derivation below. The jump matrix Λ in reciprocal space is

$$\Lambda_{mn}(\mathbf{Q}) = \nu_{mn}\exp(i\mathbf{Q}\cdot\mathbf{s}_{nm}) - \delta_{mn}\sum_{l\neq n}\nu_{nl}, \quad (4)$$

where ν_{mn} is the jump rate from site m to n, $\mathbf{Q}$ is the wave vector, δ_{mn} is the Kronecker delta, and $\mathbf{s}_{nm}$ is the jump vector from site n to site m. The neutron will transfer momentum to the hydrogen atom, corresponding to $\mathbf{Q}$. With the site probabilities $\rho_n = \exp(-\beta E_n)/\sum_m \exp(-\beta E_m)$, we construct a Hermitian jump matrix,

$$\tilde{\Lambda}(\mathbf{Q}) = \rho^{-\frac{1}{2}}\Lambda(\mathbf{Q})\rho^{\frac{1}{2}}, \quad (5)$$

where $\rho^{\frac{1}{2}}$ is a diagonal matrix of the square root of site probabilities. The jump matrix is negative definite, and its eigenvalues are negative. The incoherent scattering function is a sum of Lorentzians whose widths and weights are given by the eigenvalues $\tilde{\lambda}_i(\mathbf{Q})$ and eigenvectors $\tilde{e}_i(\mathbf{Q})$ of the Hermitian jump matrix $\tilde{\Lambda}(\mathbf{Q})$,

$$S_{\mathrm{inc}}(\mathbf{Q},\omega) = \frac{1}{\pi}\sum_{i=1}^{N_{\mathrm{sites}}} w_i(\mathbf{Q})\frac{-\hbar\tilde{\lambda}_i(\mathbf{Q})}{[\hbar\tilde{\lambda}_i(\mathbf{Q})]^2 + (\hbar\omega)^2}, \quad (6)$$

where the weights $w_i(\mathbf{Q})$ are

$$w_i(\mathbf{Q}) = \sum_l^{N_{\mathrm{sites}}}\sum_n^{N_{\mathrm{sites}}}\rho_l^{\frac{1}{2}}\tilde{e}_{in}(\mathbf{Q})\tilde{e}_{il}^*(\mathbf{Q})\rho_n^{\frac{1}{2}} = \left|\sum_l^{N_{\mathrm{sites}}}\rho_l^{\frac{1}{2}}\tilde{e}_{il}(\mathbf{Q})\right|^2. \quad (7)$$

The curvature of the incoherent scattering function $S_{\mathrm{inc}}(\mathbf{Q},\omega)$ gives the diffusivity at the small Q limit. When the diffusion occurs on a Bravais lattice, Eq. (6) simplifies to a single Lorentzian with a width $\tilde{\lambda}(\mathbf{Q})$. Equation (6) captures the full anisotropy of the scattering function; however, experiments on polycrystalline samples produce a spherically averaged $S_{\mathrm{inc}}(\mathbf{Q},\omega)$,

$$S_{\mathrm{inc}}(Q,\omega) = \iint_{4\pi}\frac{d^2\hat{\mathbf{Q}}}{4\pi}S_{\mathrm{inc}}(Q\hat{\mathbf{Q}},\omega). \quad (8)$$

The Appendix describes the numerical procedure for evaluating the spherical average. The final result is an incoherent scattering function that can be written as an integral of Lorentzians,

$$S_{\mathrm{inc}}(Q,\omega) = \int_0^\infty d\lambda\, W(Q;\lambda)\frac{1}{\pi}\frac{\hbar\lambda}{(\hbar\lambda)^2 + (\hbar\omega)^2}, \quad (9)$$

for a normalized "density of rates" $W(Q;\lambda)$. If our scattering function were represented by a Lorentzian with one width, W would be a delta function; however, we find a nontrivial distribution of rates that can only be approximated by a simple Lorentzian fit.

III. ANALYZING THE INCOHERENT SCATTERING FUNCTION

Figure 4 shows that the CE model does not capture the behavior of spherically averaged incoherent scattering function $S_{\mathrm{inc}}(Q,\omega)$ even for hydrogen in bulk palladium. The spherically averaged $S_{\mathrm{inc}}(Q,\omega)$ converges with a coarse 10×10 mesh of points on the sphere, but for the purpose of plotting the density of rates of $S_{\mathrm{inc}}(Q,\omega)$ we use a finer 100×100 mesh. We compare the density of rates of $S_{\mathrm{inc}}(Q,\omega)$ to the CE model, which assumes an isotropic jump distance and a single jump rate (or inverse mean residency time). The octahedral sites make up a Bravais lattice, but the network of octahedral and tetrahedral sites is not a Bravais lattice. The corresponding CE model uses the jump distance between octahedral sites and jump rate between octahedral sites, which is 3/4 the jump rate between an octahedral and a tetrahedral site when the tetrahedral site has a short residency time. At small Q, the density of rates of $S_{\mathrm{inc}}(Q,\omega)$ is well represented by the CE curve, which is why CE gives accurate diffusivity for bulk. However, at large Q the CE curve cannot capture the spread in the density of rates of $S_{\mathrm{inc}}(Q,\omega)$. We compare the density of rates of $S_{\mathrm{inc}}(Q,\omega)$ with analytic solutions for $S_{\mathrm{inc}}(Q,\omega)$ along particular directions. The spread in the density of rates of $S_{\mathrm{inc}}(Q,\omega)$ is bounded below by scattering along [111]-type directions, which connects neighboring octahedral and tetrahedral sites. Lorentzian terms corresponding to scattering along [110]-type directions, which connects nearest neighbor octahedral sites, have large weights. The dark band above the CE curve does not correspond to scattering along a

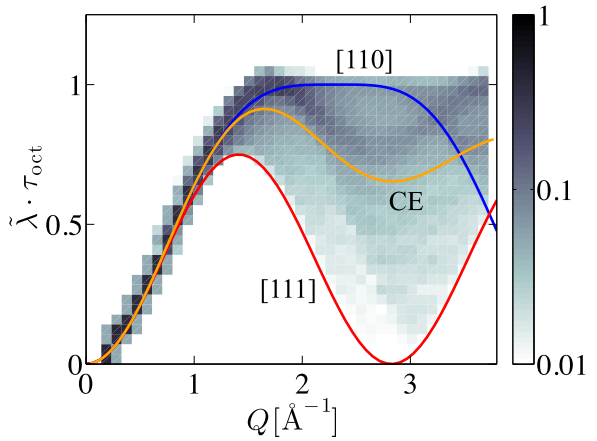

FIG. 4. Density of rates $W(Q;\lambda)$ of $S_{inc}(Q,\omega)$ for H in bulk Pd at 100 K. The gray scale indicates the weight of Lorentzian terms of widths (rates) $\tilde{\lambda}$ within a histogram bin; the sum of all weights for each Q is normalized to one. The widths are reported relative to the mean residency time in bulk, τ_{oct}. At small Q, a single width has a weight close to one because $S_{inc}(\mathbf{Q},\omega)$ is the same along all directions. At larger Q, the **Q**-directional dependence of $S_{inc}(\mathbf{Q},\omega)$ produces a range of rates with non-negligible weights. The Chudley-Elliott (CE) model cannot fully capture this spread in the density of rates of the spherically averaged scattering function $S_{inc}(Q,\omega)$. Scattering with **Q** along [111], which connects octahedral and tetrahedral sites, gives the lower bound of the distribution. Scattering with **Q** along [110], which connects nearest neighbor octahedral sites, corresponds to relatively high weights.

single direction but has contributions from several different directions.

We fit $S_{inc}(Q,\omega)$ with a single Lorentzian and use the CE model to investigate the validity of the experimentally measured jump distances and diffusivities. We try four different fitting approaches. Since the weights sum to one, the most straightforward approach is fitting a single Lorentzian with a width equal to the weighted average of the widths of the Lorentzians that make up $S_{inc}(Q,\omega)$,

$$\bar{\lambda} = \sum_i w_i \lambda_i. \tag{10}$$

This fit matches exactly for $\omega \to \infty$. The second approach is fitting a single Lorentzian of width Γ that minimizes the difference between the exact $S_{inc}(Q,\omega)$ and the single Lorentzian, i.e., that minimizes

$$\chi^2_{[0,\infty]} = \int_0^\infty \left(S_{inc}(\mathbf{Q},\omega) - \frac{\Gamma}{\pi(\Gamma^2+\omega^2)} \right)^2 d\omega. \tag{11}$$

We denote the width that minimizes this error as $\Gamma_{[0,\infty]}$. This fit favors smaller widths than the weighted average. Weighting the integrand by ω^2 gives

$$\chi^2_{\omega^2,[0,\infty]} = \int_0^\infty \omega^2 \cdot \left(S_{inc}(\mathbf{Q},\omega) - \frac{\Gamma}{\pi(\Gamma^2+\omega^2)} \right)^2 d\omega, \tag{12}$$

where terms corresponding to higher frequency contribute more to the error being minimized. We denote the width that minimizes this error as $\Gamma_{\omega^2,[0,\infty]}$. Compared to the weighted average fit, the fits obtained from $\chi^2_{[0,\infty]}$ and $\chi^2_{\omega^2,[0,\infty]}$ both favor terms with smaller widths. These three different fits have similar forms if we rewrite the equation for $\bar{\lambda}$ as

$$1 = \sum_i w_i \frac{2\lambda_i}{2\bar{\lambda}}, \tag{13}$$

the equation for $\Gamma_{[0,\infty]}$ as

$$1 = \sum_i w_i \left(\frac{2\Gamma_{[0,\infty]}}{\lambda_i + \Gamma_{[0,\infty]}} \right)^2, \tag{14}$$

and the equation for $\Gamma_{\omega^2,[0,\infty]}$ as

$$1 = \sum_i w_i \left(\frac{2\lambda_i}{\lambda_i + \Gamma_{\omega^2,[0,\infty]}} \right)^2. \tag{15}$$

A single Lorentzian would give identical widths for all fitting procedures, but a distribution of Lorentzians produces different

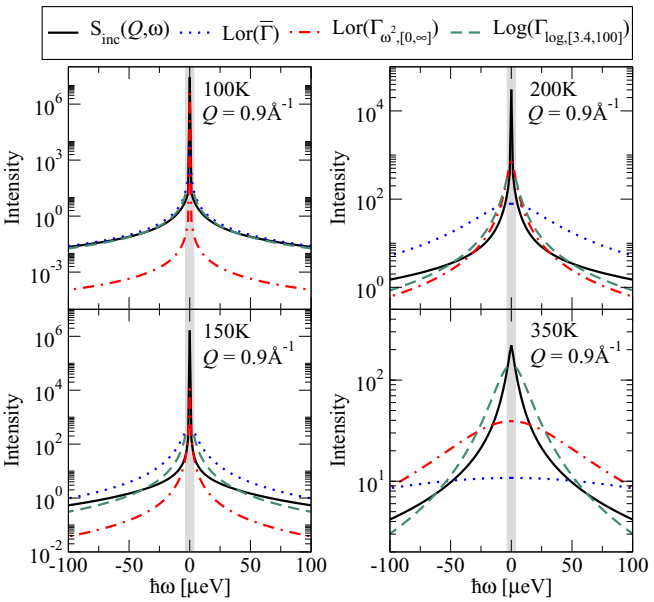

FIG. 5. Single Lorentzian fits of the analytic $S_{inc}(Q,\omega)$ as a function of neutron energy $\hbar\omega$ for $Q = 0.9$ Å^{-1} at 100, 150, 200, and 350 K for the dislocation geometry. The range of $\hbar\omega$ plotted reflects the experimental window ± 100 μeV, and the gray shading denotes energies smaller than the experimental resolution of ± 3.4 μeV. The fit to $\bar{\lambda}$ is exact for $\hbar\omega \to \infty$, and well represents $S_{inc}(Q,\omega)$ at 100 K, where the majority of the weight is distributed among terms with widths smaller than the experimental resolution. At higher temperatures, $\bar{\lambda}$ becomes a worse fit of $S_{inc}(Q,\omega)$ within the experimental window. The fit that minimizes $\chi^2_{\omega^2,[0,\infty]}$ favors smaller widths, which makes the fit poor in the range of experimentally accessible values at low temperatures. At high temperatures, both $\Gamma_{\omega^2,[0,\infty]}$ and $\bar{\lambda}$ appear to be too large in this range. The range of $\hbar\omega$ values over which $S_{inc}(Q,\omega)$ is plotted determines which of these two fits appears to be a better fit. For all temperatures, the fit that minimizes $\chi^2_{log,[3.4,100]}$, which is fit to only experimentally accessible $\hbar\omega$ values, appears to best describe $S_{inc}(Q,\omega)$ within the fixed experimental window.

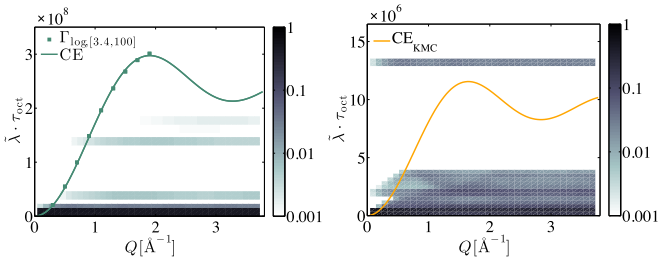

FIG. 6. Density of rates $W(Q;\lambda)$ of $S_{\rm inc}(Q,\omega)$ for the dislocation geometry at 100 K. The gray scale indicates the weight of Lorentzian terms of widths (rates) $\tilde{\lambda}$ within a histogram bin; the sum of all weights for each Q is normalized to one. The widths are reported relative to the mean residency time in bulk, $\tau_{\rm oct}$. Left: The symbols correspond to the fit widths $\Gamma_{\log,[3.4,100]}$ and the curve is the CE model fit to those widths as a function of Q. Right: The curve is the CE model using the distance between bulk nearest neighbor octahedral sites as the jump distance and diffusivity from KMC simulations, so that the curvature matches the diffusivity; note the vertical scale is two orders of magnitude smaller. Unlike the bulk case in Fig. 4, there is no single width that represents the distribution of weights even at small Q. The majority of the weight for each Q is distributed among eigenvalues that are much smaller than $\Gamma_{\log,[3.4,100]}$.

widths for the different fits. If we consider a uniform distribution of eigenvalues that extends over a range that is twice the mean width, then $\bar{\lambda}$ equals the mean width, $\Gamma_{[0,\infty]}$ is $\frac{2}{3}\bar{\lambda}$, and $\Gamma_{\omega^2,[0,\infty]}$ is $0.9307\bar{\lambda}$. Thus, $\Gamma_{[0,\infty]} < \Gamma_{\omega^2,[0,\infty]} < \bar{\lambda}$. The distribution of eigenvalues and weights from the dislocation geometry is more complicated than a uniform distribution, so we also consider an experimentlike fit over a fixed range of energies.

Experiment cannot probe $S_{\rm inc}(Q,\omega)$ for arbitrarily small or large energies or Q magnitudes. The experimental resolution, ± 3.4 μeV, and the experimental window, ± 100 μeV [9], limit the range of energies accessible in QENS experiments. Therefore, we also try a least squares fit over a fixed range. The $S_{\rm inc}(Q,\omega)$ spectra are sums of Lorentzians that span multiple orders of magnitude. To avoid having just a few sharply peaked terms in $S_{\rm inc}(Q,\omega)$ dominate the fit, we use a logarithmic least squares fit to $S_{\rm inc}(Q,\omega)$,

$$\chi^2_{\log,[3.4,100]} = \int_{3.4\ \mu{\rm eV}/\hbar}^{100\ \mu{\rm eV}/\hbar} d\omega \Bigg[\log[S_{\rm inc}(Q,\omega)] - \log\left(\frac{\Gamma}{\pi(\Gamma^2+\omega^2)}\right)\Bigg]^2, \tag{16}$$

over the same range as experimental measurements. As there is no closed-form analytic expression, we evaluate the integral using a quadrature with N_ω equally spaced ω values over the interval [3.4,100]. We denote the width that minimizes this error as $\Gamma_{\log,[3.4,100]}$, and it is the fit that best represents the experimental analysis.

Figure 5 shows that a Lorentzian of width $\Gamma_{\log,[3.4,100]}$ is the best fit to $S_{\rm inc}(Q,\omega)$ in the range of experimentally accessible energies. At low temperatures, $\bar{\lambda}$ performs better than $\Gamma_{\omega^2,[0,\infty]}$, because many of the terms with large weights have widths that are smaller than the experimental resolution. Since $S_{\rm inc}(Q,\omega)$ is sharply peaked at low temperatures, the range of experimentally accessible energies approaches the large $\hbar\omega$ limit where $\bar{\lambda}$ is exact. As temperature increases, $S_{\rm inc}(Q,\omega)$ becomes less sharply peaked. At intermediate temperatures, $\Gamma_{\omega^2,[0,\infty]}$ becomes a better representation of the part of the function that falls within the experimentally observable range. Neither $\Gamma_{\omega^2,[0,\infty]}$ nor $\bar{\lambda}$ is a good fit within the experimentally observable range of $\hbar\omega$ for the entire range of temperatures.

Figures 6 and 7 show that neither $\Gamma_{\log,[3.4,100]}$ nor CE fits to $\Gamma_{\log,[3.4,100]}$ capture physical rates that dominate $S_{\rm inc}(Q,\omega)$, but $\Gamma_{\log,[3.4,100]}$ matches well with the widths from experiment for deformed palladium. The spread of the density of rates of $S_{\rm inc}(Q,\omega)$ for hydrogen in the dislocation cannot be captured by a single Lorentzian width even at small Q. At 100 K, $\Gamma_{\log,[3.4,100]}$ is over an order of magnitude larger than the highest weighted widths. This corroborates with Fig. 5 that at low temperatures the widths with the largest weight are smaller than the experimental resolution and are not represented by $\Gamma_{\log,[3.4,100]}$. The CE model parametrized with the diffusivity from KMC and the distance between nearest neighboring octahedral sites in bulk spans a smaller range of widths that falls closer to the higher weighted widths. However, Fig. 6 shows that the spread in the density of rates of $S_{\rm inc}(Q,\omega)$ cannot be described as a single width. The density of rates of $S_{\rm inc}(Q,\omega)$

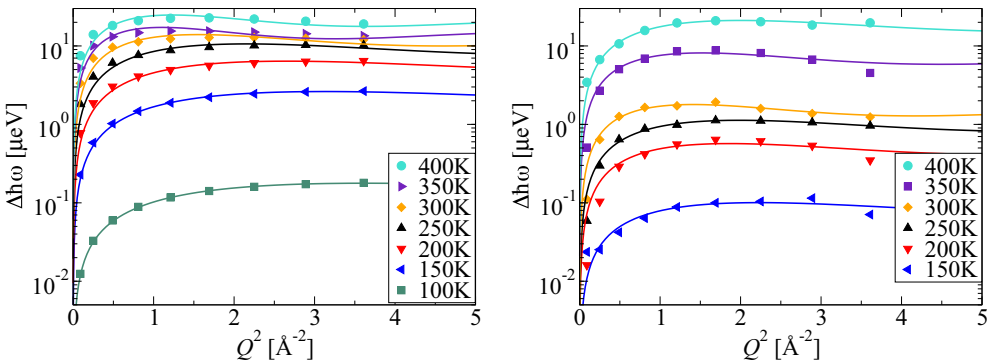

FIG. 7. Chudley-Elliott fit to the widths of $S_{\rm inc}(Q,\omega)$ for the dislocation geometry. Left: The symbols correspond to $\Gamma_{\log,[3.4,100]}$ and the lines are CE fits to those widths for each temperature. The CE model captures the trend of the fitted widths as a function of Q. The widths from the least squares fit of $\log[S_{\rm inc}(Q,\omega)]$ vary across the same orders of magnitude for increasing temperatures as seen in experiment [9] (right).

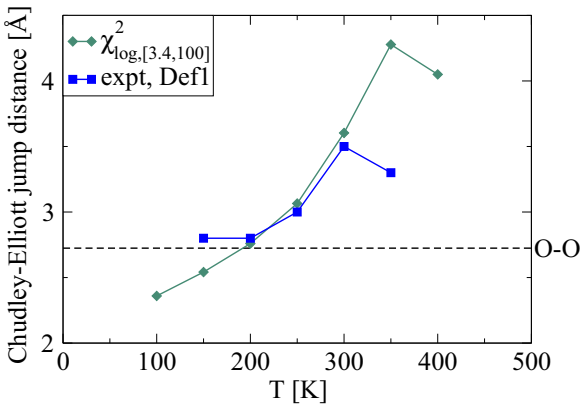

FIG. 8. Jump distance as a function of temperature. The computed jump distances from CE fits to $\Gamma_{\log,[3.4,100]}$ vary nonmonotonically and span the same range as found in experiment [9]. For comparison, the distance between two octahedral sites in bulk ≈2.724 Å, and the distance between an octahedral site and a tetrahedral site ≈1.668 Å.

features large gaps between eigenvalues with large weights, because the spectrum of rates is not continuous. In bulk, there are only two rates ν_{OT} and ν_{TO}, while the dislocation produces a range of rates. As temperature increases, the relative size of these gaps decreases. The trend of $\Gamma_{\log,[3.4,100]}$ is well described by the CE model for all temperatures in Fig. 7(a). Even though $\Gamma_{\log,[3.4,100]}$ is a poor representation of $S_{\mathrm{inc}}(Q,\omega)$, we find good agreement between $\Gamma_{\log,[3.4,100]}$ and the experimental widths in Fig. 7(b) by using the same fitting approach. As with experiment, we can extract a mean residence time and an average jump distance for each temperature from these fits to the Chudley-Elliott model, and make a model of diffusivity that we can compare with the direct KMC diffusivity values.

Figure 8 shows that the jump distances extracted from the CE fits to $\Gamma_{\log,[3.4,100]}$ are nonmonotonic as a function of temperature and larger than distances in our dislocation geometry at higher temperatures, similar to those found by experiment. Jump distances between nearest neighbor octahedrals in the expanded region below the core, ∼2.74 Å, are less than 1% larger than the nearest neighbor octahedral distance in bulk. In the core, the interstitial sites are sheared, and it is difficult to classify these sites as octahedral or tetrahedral sites. However, the jump distances between every other site are similar to the nearest neighbor octahedral site distances below the core. The distance between each site in the core alternates between ∼1.43 and ∼1.62 Å. Distances between sites in the core that connect to sites in the expanded region below the core are either ∼0.95 or ∼1.59 Å. None of these distances account for the large jump distances extracted from the CE model and $\chi^2_{\log,[3.4,100]}$. Rather, it suggests the behavior is an artifact of the fitting procedure.

Figure 9 shows that the experimentlike fit $\chi^2_{\log,[3.4,100]}$ yields a diffusion barrier that is lower than the KMC diffusion barrier. From our KMC simulations we find an effective diffusion barrier of $E_a = 0.125$ eV. The diffusion barrier obtained from a CE fit to $\Gamma_{\log,[3.4,100]}$ is $E_a = 0.068$ eV, which matches the experimentally observed diffusion barrier [9]. Depending on temperature, different Lorentzian terms dominate $S_{\mathrm{inc}}(Q,\omega)$

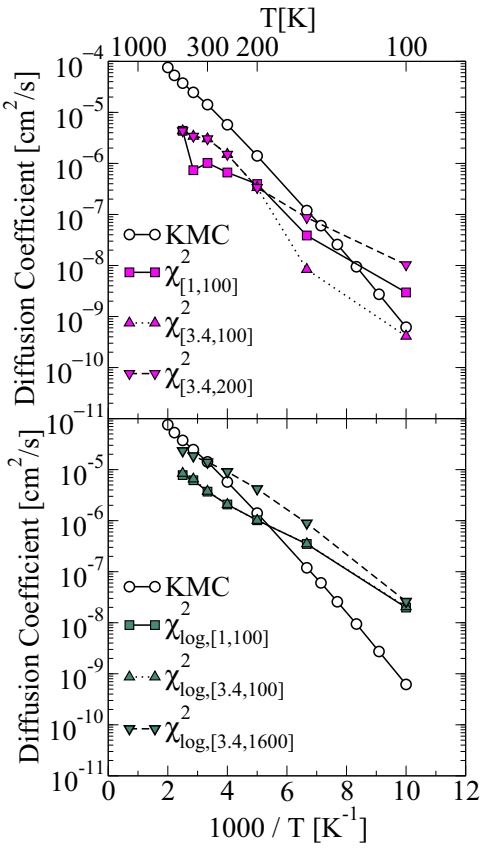

FIG. 9. Diffusivities extracted from CE fits compared to diffusivity extracted from kinetic Monte Carlo simulations. The error bars of the KMC data points are smaller than the symbol sizes. A linear least squares fit over experimentally accessible energies $\chi^2_{[3.4,100]}$ underpredicts diffusivity and is noisy due to widths as a function of Q that are not well described by the CE model. Increasing the experimental window $\chi^2_{[3.4,200]}$ and decreasing the experimental resolution $\chi^2_{[1,100]}$ predict slightly different diffusivities, but neither leads to better agreement with KMC. The diffusion barrier from the experimentlike fit $\chi^2_{\log,[3.4,100]}$ is smaller than the diffusion barrier from KMC simulations, because $\chi^2_{\log,[3.4,100]}$ overpredicts diffusivity at low temperature but underpredicts diffusivity at high temperature. A smaller experimental resolution $\chi^2_{\log,[1,100]}$ has no effect on the extracted diffusivity. A larger experimental window $\chi^2_{\log,[3.4,1600]}$ predicts slightly different diffusivity but still does not improve agreement with the diffusivity obtained from KMC.

in the fixed range of [3.4,100]. The lower diffusion barrier is a result of the $\chi^2_{\log,[3.4,100]}$ fit overpredicting diffusivity at low temperatures and underpredicting diffusivity at high temperatures. One might think that increasing the range of energies over which we fit $S_{\mathrm{inc}}(Q,\omega)$ would improve the accuracy of the extracted diffusivity. However, we find that including lower energies in the fitting range [1,100] has little effect on the diffusivity. As we extend the experimental window from 100 to 1600 μeV ($\chi^2_{\log,[3.4,100]}$ to $\chi^2_{\log,[3.4,1600]}$), the extracted diffusivity approaches the diffusivity from $\bar{\lambda}$, which does not agree with the diffusivity from KMC simulations. We also compare these values to a linear least squares fit over the range of experimentally accessible energies, which is more sensitive to changes in the lower limit of the energy range.

Using this linear least squares fit, the widths as a function of Q are not well described by the CE model for any range of energies, especially for high temperatures, which leads to poor predictions of diffusivity.

IV. CONCLUSION

This work illustrates two major conclusions. First, DFT is able to quantitatively predict pipe diffusion and is consistent with experiment. We find low diffusion barriers from sites in the expanded region below the partial core into the partial core and a diffusion pathway inside the partial core with low diffusion barriers. This pathway allows diffusing hydrogen atoms to bypass other hydrogen atoms by moving from the lowest energy states below the partial cores to slightly higher energy states inside the partial cores. Second, traditional analysis of QENS spectra, i.e., representing $S_{\text{inc}}(\mathbf{Q},\omega)$ as a single Lorentzian and using a Chudley-Elliott model to extract diffusivities, oversimplifies the data and leads to errors in the diffusivity. Furthermore, these errors are difficult to detect using experimental data alone. The Chudley-Elliott model matches the trend of the experimental widths as a function of Q and leads to an Arrhenius relationship between the model diffusivity and temperature. Only the jump distance as a function of temperature behaves unusually. Fixing the jump distance to be the bulk distance between nearest neighbor octahedral sites produces worse fits of the experimental widths as a function of Q but has little effect on the model diffusivity. The deviation between the diffusivity we calculate with KMC and those we calculate using an experimentlike fit differs by more than what could be accounted for by differences between the fitted jump distances from experiment and bulk jump distances. Experiments need to be compared to the incoherent scattering function directly using a computational model that can predict the incoherent scattering function and diffusivity. This approach is general and could be applied to other systems with anisotropic diffusion, such as diffusion near grain boundaries and interfaces.

ACKNOWLEDGMENTS

This research was funded by NSF under Grant No. DMR-1207102. This work used the Extreme Science and Engineering Discovery Environment (XSEDE) [34], which is supported by National Science Foundation Grant No. ACI-1053575 at the Texas Advanced Computing Center; and the Taub cluster at the University of Illinois, Urbana-Champaign.

APPENDIX: SPHERICAL AVERAGING

We evaluate $S_{\text{inc}}(\mathbf{Q},\omega)$ on a spherical grid of points to compute the spherical average. We use uniformly spaced points for ϕ from 0 to 2π. For θ, we use one-dimensional Gauss quadrature, specifically, Gauss-Legendre nodes with weights c_i [35]. The Gauss-Legendre nodes span the interval $[-1,1]$. We take the inverse cosine of the nodes to get θ points that span 0 to π. Our expression for the approximate integral is

$$S_{\text{inc}}(Q,\omega) \approx \frac{1}{N_\phi} \sum_{j=1}^{N_\phi} \sum_{i=1}^{N_\theta} c_i \cdot S_{\text{inc}}[\mathbf{Q}(\theta_i,\phi_j),\omega], \tag{A1}$$

where N_θ and N_ϕ are the number of grid points.

[1] D. Turnbull and R. E. Hoffman, Acta Metall. **2**, 419 (1954).
[2] E. W. Hart, Acta Metall. **5**, 597 (1957).
[3] G. R. Love, Acta Metall. **12**, 731 (1964).
[4] T. E. Volin, K. H. Lie, and R. W. Balluffi, Acta Metall. **19**, 263 (1971).
[5] X. Tang, K. P. D. Lagerlöf, and A. H. Heuer, J. Am. Ceram. Soc. **86**, 1560 (2003).
[6] M. Legros, G. Dehm, E. Arzt, and T. J. Balk, Science **319**, 1646 (2008).
[7] H. Kimizuka and S. Ogata, Phys. Rev. B **84**, 024116 (2011).
[8] D. R. Trinkle, H. Ju, B. J. Heuser, and T. J. Udovic, Phys. Rev. B **83**, 174116 (2011).
[9] B. J. Heuser, D. R. Trinkle, N. Jalarvo, J. Serio, E. J. Schiavone, E. Mamontov, and M. Tyagi, Phys. Rev. Lett. **113**, 025504 (2014).
[10] C. T. Chudley and R. J. Elliott, Proc. Phys. Soc. **77**, 353 (1961).
[11] Y. Li and G. Wahnström, Phys. Rev. Lett. **68**, 3444 (1992).
[12] Y. Li and G. Wahnström, Phys. Rev. B **46**, 14528 (1992).
[13] J. M. Rowe, J. J. Rush, L. A. deGraaf, and G. A. Ferguson, Phys. Rev. Lett. **29**, 1250 (1972).
[14] M. J. Gillan, J. Phys. C **19**, 6169 (1986).
[15] M. E. Björketun, P. G. Sundell, G. Wahnström, and D. Engberg, Solid State Ionics **176**, 3035 (2005).
[16] J. M. Rowe, K. Sköld, H. E. Flotow, and J. J. Rush, J. Phys. Chem. Solids **32**, 41 (1971).
[17] K. W. Kehr, D. Richter, and R. H. Swendsen, J. Phys. F **8**, 433 (1978).
[18] J. W. Haus and K. W. Kehr, Phys. Rep. **150**, 263 (1987).
[19] R. Hempelmann, *Quasielastic Neutron Scattering* (Oxford University Press, Oxford, U.K., 2000).
[20] F. E. Tuddenham, H. Hedgeland, A. P. Jardine, B. A. J. Lechner, B. J. Hinch, and W. Allison, Surf. Sci. **604**, 1459 (2010).
[21] S. Paterson, C. J. Aas, and A. P. Jardine, Surf. Sci. **606**, 426 (2012).
[22] C. J. Carlile and D. K. Ross, Solid State Commun. **15**, 1923 (1974).
[23] G. Kresse and J. Hafner, Phys. Rev. B **47**, 558 (1993).
[24] G. Kresse and J. Furthmüller, Phys. Rev. B **54**, 11169 (1996).
[25] P. E. Blöchl, Phys. Rev. B **50**, 17953 (1994).
[26] G. Kresse and D. Joubert, Phys. Rev. B **59**, 1758 (1999).
[27] H. M. Lawler and D. R. Trinkle, Phys. Rev. B **82**, 172101 (2010).
[28] J. A. Rayne, Phys. Rev. **118**, 1545 (1960).
[29] Y. M. Koroteev, O. Gimranova, and I. Chernov, Phys. Solid State **53**, 896 (2011).

[30] G. Henkelman, B. P. Uberuaga, and H. Jonsson, J. Chem. Phys. **113**, 9901 (2000).
[31] J. Völkl and G. Alefeld, in *Hydrogen in Metals I*, Topics in Applied Physics Vol. 28 (Springer, Berlin, 1978), Chap. 12, pp. 321–348.
[32] J. A. Yasi, L. G. Hector, Jr., and D. R. Trinkle, Acta Mater. **58**, 5704 (2010).
[33] H. Grönbeck and V. P. Zhdanov, Phys. Rev. B **84**, 052301 (2011).
[34] J. Towns, T. Cockerill, M. Dahan, I. Foster, K. Gaither, A. Grimshaw, V. Hazlewood, S. Lathrop, D. Lifka, G. Peterson, R. Roskies, J. Scott, and N. Wilkins-Diehr, Comput. Sci. Eng. **16**, 62 (2014).
[35] G. H. Golub and J. H. Welsch, Math. Computation **23**, 221 (1969).